AGU PUBLICATIONS

JGR

Journal of Geophysical Research: Atmospheres

RESEARCH ARTICLE
10.1002/2017JD028009

Key Points:
- We constrain anthropogenic NO_x emissions by Kalman filter using the NO_2 observations from GCAS sensor
- Constrained emissions counterbalance the well-documented positive bias of 1×1 km^2 regional model against surface observations
- GCAS provides a unique opportunity to detect and constrain an emission event anomaly in the Houston area

Correspondence to:
Y. Choi,
ychoi6@uh.edu

Citation:
Souri, A. H., Choi, Y., Pan, S., Curci, G., Nowlan, C. R., Janz, S. J., et al. (2018). First top-down estimates of anthropogenic NO_x emissions using high-resolution airborne remote sensing observations. *Journal of Geophysical Research: Atmospheres*, *123*, 3269–3284. https://doi.org/10.1002/2017JD028009

Received 4 NOV 2017
Accepted 2 MAR 2018
Accepted article online 7 MAR 2018
Published online 25 MAR 2018

First Top-Down Estimates of Anthropogenic NO_x Emissions Using High-Resolution Airborne Remote Sensing Observations

Amir H. Souri[1], Yunsoo Choi[1], Shuai Pan[1], Gabriele Curci[2,3], Caroline R. Nowlan[4], Scott J. Janz[5], Matthew G. Kowalewski[5,6], Junjie Liu[7], Jay R. Herman[5,8], and Andrew J. Weinheimer[9]

[1]Department of Earth and Atmospheric Sciences, University of Houston, Houston, TX, USA, [2]CETEMPS, University of L'Aquila, L'Aquila, Italy, [3]Department of Physical and Chemical Sciences, University of L'Aquila, L'Aquila, Italy, [4]Harvard-Smithsonian Center for Astrophysics, Cambridge, MA, USA, [5]NASA Goddard Space Flight Center, Greenbelt, MD, USA, [6]Goddard Earth Sciences Technology and Research, USRA, Greenbelt, MD, USA, [7]Jet Propulsion Laboratory, Caltech, Pasadena, CA, USA, [8]Joint Center for Earth Systems Technology, University of Maryland, Baltimore County, Baltimore, MD, USA, [9]National Center for Atmospheric Research, Boulder, CO, USA

Abstract A number of satellite-based instruments have become an essential part of monitoring emissions. Despite sound theoretical inversion techniques, the insufficient samples and the footprint size of current observations have introduced an obstacle to narrow the inversion window for regional models. These key limitations can be partially resolved by a set of modest high-quality measurements from airborne remote sensing. This study illustrates the feasibility of nitrogen dioxide (NO_2) columns from the Geostationary Coastal and Air Pollution Events Airborne Simulator (GCAS) to constrain anthropogenic NO_x emissions in the Houston-Galveston-Brazoria area. We convert slant column densities to vertical columns using a radiative transfer model with (i) NO_2 profiles from a high-resolution regional model (1×1 km^2) constrained by P-3B aircraft measurements, (ii) the consideration of aerosol optical thickness impacts on radiance at NO_2 absorption line, and (iii) high-resolution surface albedo constrained by ground-based spectrometers. We characterize errors in the GCAS NO_2 columns by comparing them to Pandora measurements and find a striking correlation ($r > 0.74$) with an uncertainty of 3.5×10^{15} molecules cm^{-2}. On 9 of 10 total days, the constrained anthropogenic emissions by a Kalman filter yield an overall 2–50% reduction in polluted areas, partly counterbalancing the well-documented positive bias of the model. The inversion, however, boosts emissions by 94% in the same areas on a day when an unprecedented local emissions event potentially occurred, significantly mitigating the bias of the model. The capability of GCAS at detecting such an event ensures the significance of forthcoming geostationary satellites for timely estimates of top-down emissions.

1. Introduction

Nitrogen dioxide (NO_2) is an important air pollutant from anthropogenic and natural sources (Brewer et al., 1973). Current estimates of anthropogenic emissions contributing to NO_2 are primarily based on bottom-up inventories associated with large uncertainties resulting from errors in underlying assumptions and county-level statistics. If we optimistically assume that they reflect real emissions for a certain year, the frequency of updates is still lower than that of changes in emissions. Thus, NO_x ($NO + NO_2$) emissions can sometimes be overestimated by a factor of 2, especially in the southeastern United States (Souri et al., 2016; Travis et al., 2016). One way to improve the accuracy of emissions estimates is to minimize the distance between observed NO_2 observations and simulated values based on bottom-up emissions.

NO_2 molecules have strong absorption of UV radiation, so their retrieval is one of the most successfully detected species from remote sensing (Boersma et al., 2004; Nowlan et al., 2016). The availability of NO_2 columns from several spaceborne satellites in conjunction with chemical transport models has enabled the use of inverse modeling in constraining NO_x emissions around the world (Chai et al., 2009; Ding et al., 2017; Jaeglé et al., 2005; Martin et al., 2003; Mijling et al., 2017; Mijling & van der A, 2012; Miyazaki et al., 2012, 2017; Qu et al., 2017; Souri et al., 2016, 2017).

Similar to several types of spectrometer instruments, sensors and optics used in satellites are subject to degradation. For instance, since 2009, almost half a row of Ozone Monitoring Instrument (OMI) detectors

encompassing the spatially finest resolution pixels (~13 × 24 km^2) have been complicated by a row anomaly. The deficiencies of current sensors are not only limited to instrumental degradation but also result from coarse temporal and spatial resolutions, which prevent us from investigating uncertainties in emissions or the chemical and physical processes involved on a fine scale. Therefore, to resolve emissions on a regional scale, we resort to spatially oversampling observations, which in turn, potentially average out some temporal information. For example, although Souri et al. (2016), using the OMI satellite in September 2013, successfully mitigated the positive bias of a model to reproduce surface NO_2, they failed to correct large underpredictions of the model between 24 and 26 September, when an anomaly in emissions potentially occurred.

Fortunately, future sensors (e.g., Zoogman et al., 2017) should address these shortcomings by providing higher resolutions. Until they are in operation, however, there is an urgent need to examine whether utilizing high-quality observations can induce greater accuracy in emissions estimates in a timely manner. Several airborne remote sensing sensors such as the Airborne Compact Atmospheric Mapper (Lamsal et al., 2017), Geostationary Trace Gas and Aerosol Sensor Optimization (Nowlan et al., 2016), and the Geostationary Coastal and Air Pollution Events Airborne Simulator (GCAS) (Kowalewski & Janz, 2014) provide high-resolution gas columns (<~1 km) with useful signal-to-noise ratios. Unfortunately, these valuable data have not been used for constraining emissions in many applications. Accordingly, the motivation for this study is the opportunity to investigate the possibility of using GCAS NO_2 vertical column densities (VCDs), for the first time, to improve 1 km anthropogenic emissions in Houston-Galveston-Brazoria (HGB) during the Deriving Information on Surface Conditions from COlumn and VERtically Resolved Observations Relevant to Air Quality (DISCOVER-AQ) campaign of National Aeronautics and Space Administration (NASA).

2. Measurements, Modeling, and Method

2.1. GCAS

An Offner design spectrometer flew as part of the GCAS system on NASA B200 aircraft (altitude ~8 km) to collect ultraviolet-visible spectrophotometry range (300–490 nm) images with a spectral resolution of 0.6 nm (Kowalewski & Janz, 2014). The data were acquired for 11 days in September 2013 from ~8 a.m. to ~4 p.m. local time. The last day of observations (27 September) was not considered in this study due to relatively fewer number of samples on this specific day. The GCAS ground footprint size is a function of the altitude, the aircraft speed, scan range, and the sensor aperture. Moreover, we coadded the spectra spatially to meet the GCAS signal-to-noise requirements. Accordingly, the combination of the sensor geometry and spatially averaged spectra during the DISCOVER-AQ campaign resulted in a spatial resolution of ~250 m × 500 m, which was 2,500 times as fine as that of the OMI nadir pixels. The NO_2 absorption range of 420 to 465 nm was selected, and subsequently, the NO_2 slant column was fit using direct radiance fitting (Chance, 1998). The spectral fit method requires a solar irradiance spectrum as a reference; that is, the slant column density (SCD) retrieved from the method yields differential NO_2 with respect to the SCD at the reference location. While satellite-borne sensors provide a reference spectrum taken outside the atmosphere directly from the Sun, GCAS was only able to provide a reference spectrum determined using nadir observations. We estimated the reference spectrum by averaging several GCAS-derived spectra over a relatively unpolluted region in the Gulf of Mexico as a function of cross-track position (21 lines in total). We used a single spectrum for the entire campaign to make sure that all data had the same background correction. The dependence of the cross-track position eliminated cross-track striping and potential biases (Nowlan et al., 2016).

In this analysis, we masked any pixel whose error of fit was greater than half of the SCD based, a commonly used decision rule for a normal distribution with a 95% confidence level. We labeled a pixel cloudy if the mean radiance in the NO_2 fitting window exceeded a threshold of 2×10^{13} photons cm^{-2} $nm^{-1}s^{-1}$ sr^{-1}.

2.2. Aircraft

We used the latest version of P-3B NO_2 data collected by the National Center for Atmospheric Research in situ four-channel chemiluminescence instrument (Ridley & Grahek, 1990; Ridley et al., 2004). These data were available for 10 flight days during the campaign. The frequency of NO_2 sampling was 1 s.

2.3. Pandora Spectrometer Instrument

This study used data from Pandora Spectrometer Instrument (PSI) ground-based spectrometers at 11 stations. The spectrometer generates total NO_2 columns with a clear-sky precision of 2.7×10^{14} molecules cm^{-2}

(0.01 DU) and a nominal accuracy of 2.7×10^{15} molecules cm^{-2} (0.1 DU) (Herman et al., 2009). We filtered out the observations with an error of >0.05 DU. It should be noted that the PSI retrieval lacked a direct separation of tropospheric and stratospheric NO_2 columns.

2.4. Ambient Surface Monitoring Stations

Hourly NO_2 measurements were gathered from Continuous Ambient Monitoring Stations and Air Quality System sites. Our domain model contained 29 stations. Not all observations were available for a given day. Unlike the P-3B, NO_2 observations required correction resulting from interference from several reactive nitrogen gases. We mitigated this contamination using a method developed by Lamsal et al. (2008) by incorporating a chemical transport model.

2.5. Weather Research and Forecasting-Community Multiscale Air Quality

We conducted a simulation using the U.S. Environmental Protection Agency (EPA) Community Multiscale Air Quality (CMAQ) model (Byun & Schere, 2006), version 5.0.2, which provides a priori NO_2 profiles (i) to estimate air mass factors (AMFs), (ii) to bridge observations to emissions for inverse modeling, and (iii) to verify the accuracy of a priori and a posteriori NO_x emissions. Our model consisted of three domains: the parent domain, with a 12 km spatial resolution covering the entire United States and two inner domains, with 4.0 and 1.0 km grid sizes, covering southeastern Texas and HGB, respectively. The vertical grid included 27 pressure-sigma levels stretching from the near surface to ~20 km. We selected the CB05 gas-phase and six-generation aerosol mechanisms. CMAQ used meteorological fields from the Advanced Research Weather Research and Forecasting (WRF) v3.7 model (Skamarock & Klemp, 2008). The WRF configuration and performance against surface observations were similar to those in the study of Pan, Choi, Jeon, et al. (2017), who found that the model and observations agreed within 0.9°C for surface temperature and 1 m/s for wind speed. Despite the fact that the WRF setup fairly reproduced surface wind fields during the campaign (Pan, Choi, Jeon, et al., 2017), their uncertainties are a potential source of errors in estimating top-down emissions (Liu et al., 2017), particularly those emission sectors which are far from major sources.

The period of simulation covered the last week of August for a spin-up and all of September 2013. We applied the Sparse Matrix Operator Kernel Emissions and the Motor Vehicle Emissions Simulator models based on the 2011 platform (v6.1) to generate anthropogenic emissions and the Biogenic Emission Inventory System version 3 to generate biogenic emissions. Studies have thoroughly investigated the performance of our CMAQ model against surface and aircraft observations (Pan, Choi, Jeon, et al., 2017; Pan, Choi, Roy, & Jeon, 2017). The discrepancy between model and observations in terms of NO_2 will be discussed in more detail later. Figure 1 depicts the model domain and all in situ observations used in this study.

2.6. AMF Calculations

To constrain anthropogenic NO_x emissions using the GCAS NO_2 SCD, we had to prepare observations so that the forward model can project them onto state vectors (i.e., emissions). Thus, we needed to convert the SCD into VCD, which is generally done by

$$\mathrm{AMF} = \frac{\mathrm{SCD}}{\mathrm{VCD}} = \frac{\tau_S}{\tau_V}, \tag{1}$$

where τ_S and τ_V represent the unitless optical thicknesses for the slant and vertical columns, respectively, which require a quantity of absorbed and scattered ultraviolet-visible spectrophotometry radiance along the two pathways. In the absence of any absorption and scattering, we simplify the AMF to the geometric AMF (AMF_G)

$$\mathrm{AMF}_G = \sec\theta_s + \sec\theta_v, \tag{2}$$

where θ_s is the solar zenith and θ_v the sensor viewing angles. For instance, at a point where the Sun or the sensor is close to the horizon (i.e., a deeper look into the atmosphere), the SCD will become significantly larger than the VCD. In reality, atmospheric gases and particles interfere with the light path, and we must derive the AMF from the Beer-Lambert law of extinction (Palmer et al., 2001):

$$\mathrm{AMF} = \mathrm{AMF}_G \int_{\sigma_o}^{1} \overbrace{-\frac{1}{\mathrm{AMF}_G}\frac{\alpha(\sigma)}{\alpha_e}\frac{\partial \ln I_B}{\partial \tau}}^{w(\sigma)} \times \overbrace{\frac{\Omega_a}{\Omega_v}\eta(\sigma)}^{S(\sigma)} \mathrm{d}\sigma, \tag{3}$$

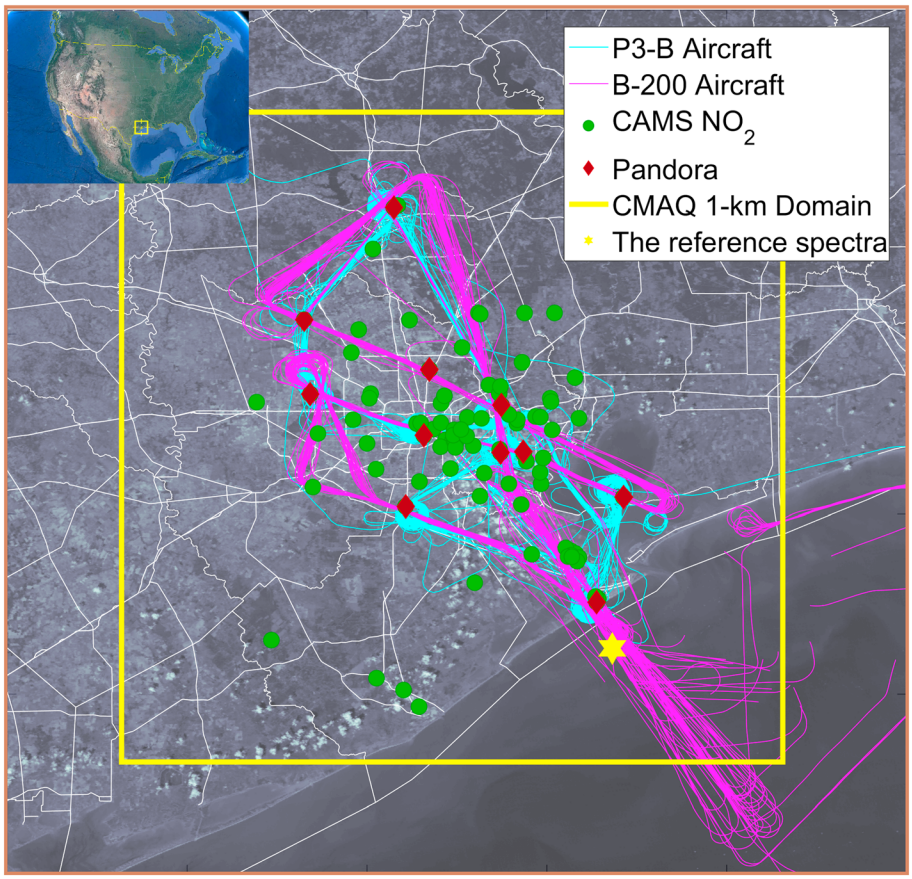

Figure 1. National Aeronautics and Space Administration Moderate Resolution Imaging Spectroradiometer AQUA on 25 September 2013, showing the location of surface and aircraft observations and the high-resolution (1 km) Community Multiscale Air Quality (CMAQ) domain. The reference spectra location, presented as a star, was used for the retrieval of Geostationary Coastal and Air Pollution Events Airborne Simulator NO_2 slant columns. CAMS = Continuous Ambient Monitoring Stations.

where $w(\sigma)$ and $S(\sigma)$ are scattering weights (SWs) and shape factors (SFs) at the sigma (σ) vertical coordinate, σ_0 is the sigma level at the altitude of an aircraft, $\alpha(\sigma)$ is the absorption of the cross section, α_e is the effective cross section at 432 nm, and I_B is the radiance observed by the sensor. The SF is estimated by the ratio of the vertical column of air, $\Omega_a(\sigma)$, to the vertical column of NO_2 and the mixing ratio of the a priori profile of NO_2 from the model. To estimate the partial derivative of the radiance to the optical thickness ($\frac{\partial \ln I_B}{\partial \tau}$), we used the linearized discrete ordinate radiative transfer (LIDORT) 3.7 model (Spurr, 2008). This radiative transfer model (RTM) requires several inputs such as aerosol optical depth (AOD), surface albedo, and sensor geometry. With regard to surface albedo, we used the Moderate Resolution Imaging Spectroradiometer (MODIS) bidirectional reflectance distribution function (BRDF) channel 3 (470 nm). The RTM treats all BRDF quantities with respect to surface properties using a linear combination of BRDF kernels. To compute aerosol-specific AOD, we ran the Flexible Aerosol Optical Depth postprocessing toolbox (Curci et al., 2015), which is based on Mie's scattering model, at 432 nm from the CMAQ output for five categories: dust, black carbon, organic carbon, sulfate, and sea salt. A general overview of the AMF calculation is shown in the left panel of Figure 2.

As mentioned earlier, the spectral fit algorithm estimated the SCD with respect to a reference spectrum. This reference spectrum may be obtained by collecting the extraterrestrial sunlight spectrum, as done in several spaceborne observations such as OMI, in which case equation (1) was applicable. However, for the GCAS case, we selected an earthshine spectrum over the Gulf of Mexico (depicted in Figure 1) and estimated the VCD below the aircraft by the following equation:

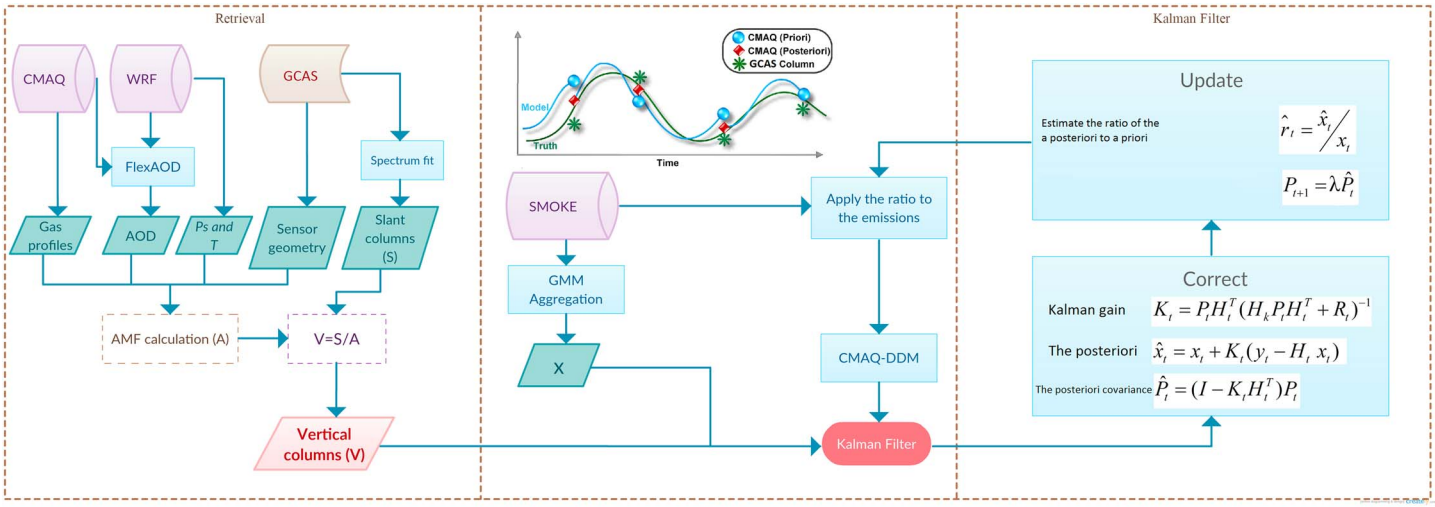

Figure 2. Schematic of the retrieval process and the inversion in this study design. The main purpose of the retrieval process is to provide vertical NO_2 columns. The values, along with the aggregated anthropogenic NO_x emissions, are provided to the Kalman filter, which carries out the inversion. The Kalman filter estimates the a posteriori emissions by minimizing the cost function. Subsequently, the ratio of the a posteriori to a priori emissions is applied to the emissions. The covariance matrix of the a priori values changes over time, depending on the previous estimation error and the inflation factor (λ). CMAQ = Community Multiscale Air Quality; WRF = Weather Research and Forecasting; GCAS = Geostationary Coastal and Air Pollution Events Airborne Simulator; FlexAOD = Flexible Aerosol Optical Depth; AOD = aerosol optical depth; AMF = air mass factor; SMOKE = Sparse Matrix Operator Kernel Emissions; GMM = Gaussian mixture model; DDM = Direct Decoupled Model.

$$\mathrm{VCD}_{\downarrow} = \frac{\mathrm{SCD} - \mathrm{VCD}_{\uparrow} \times \mathrm{AMF}_{\uparrow} + \left(\mathrm{VCD}^{R}_{\uparrow} \times \mathrm{AMF}^{R}_{\uparrow} + \mathrm{VCD}^{R}_{\downarrow} \times \mathrm{AMF}^{R}_{\downarrow}\right)}{\mathrm{AMF}_{\downarrow}}, \tag{4}$$

where the arrows denote values above (↑) or beneath (↓) the aircraft and *R* represents the quantities at the reference location (Lamsal et al., 2017; Nowlan et al., 2016). All of the VCDs in the right side of the equation were estimated from the regional model. Since the reference spectra were collected close to the location of target observations, the second and third terms were virtually similar. This suggests that the SCD (first term) should be added to that of beneath the aircraft over the reference location (fourth term) to represent the absolute SCD (rather than the relative SCD).

2.7. Inversion Method

NO_x emissions are not directly observed from GCAS. Thus, to derive quantitative constraints on emissions, we used inverse modeling to incorporate NO_2 columns into our knowledge about the chemical and physical processes that take place in these two quantities. Here our observations were the GCAS NO_2 VCDs, and the unknowns were the corresponding NO_x emissions. We based the inversion system on a Kalman filter, which is analogous to the sequential Bayesian method fully described in Souri et al. (2016, 2017).

Assuming that observation and unknown errors follow the Gaussian distribution and that their relationship is linear, we estimate the a posteriori values by minimizing the following cost function from Bayes's theorem (Rodgers, 2000) as follows:

$$J(\boldsymbol{x}) = \frac{1}{2}(\boldsymbol{y} - H\boldsymbol{x})^T \mathbf{R}^{-1}(y - H\boldsymbol{x}) + \frac{1}{2}(\boldsymbol{x} - \boldsymbol{x}_a)^T \mathbf{P}^{-1}(\boldsymbol{x} - \boldsymbol{x}_a), \tag{5}$$

where $\boldsymbol{x}$ is unknown (i.e., a state vector), $\boldsymbol{y}$ represents GCAS NO_2 VCDs, $\mathbf{P}$ and $\mathbf{R}$ are the covariance matrices of the a priori values and observations, respectively, and *H* is the Jacobian matrix explaining the relationship of observations to unknowns. To calculate the *H* matrix, we used the CMAQ-Direct Decoupled Model (DDM), which estimates the locally seminormalized gradients of NO_2 to NO_x emissions (Cohan et al., 2005) and assumed a 50% error in emissions (Huang et al., 2014; Souri et al., 2016, 2017). Later on, we will compute the uncertainty of the GCAS NO_2 VCDs by comparing them to ground truth. It is worth noting that we optimized log($\boldsymbol{x}$) rather than $\boldsymbol{x}$ to add a hidden constraint; that is, the a posteriori values should always be positive.

To increase the degree of freedom for minimizing the cost function and to partially consider the impact of transport on the misalignment between the source and the receptor, we aggregate the emissions using

the Gaussian mixture model (GMM) which was thoroughly described in Bishop (2007). The inputs for this classifier were all of the emission sectors as well as the latitude and the longitude of the domain and urban/water fractions based on a land use/land cover map. Unlike a widely used method called K-means, the GMM algorithm requires an assumption on the probability structure of the data. Each zone for the inversion was mathematically represented by a normal distribution. First, a mixture of parametric Gaussian distributions was randomly spread over the feature space, and the probability of the data generated by each of the Gaussians was determined. Second, each data point was assigned to the zone which yielded the maximum probability. Subsequently, the algorithm was iteratively applied to all data points; the normal distribution parameters were recalculated and so on until a convergence. During recalculation of the normal distribution parameters, we sometimes observed that a fitted covariance matrix became ill conditioned. As a remedy, we enhanced slightly all the covariance matrices by 0.001 (i.e., regularization) at a cost of reducing the maximum likelihood of estimation.

By obtaining the first derivative of equation (5), we estimated the a posteriori emissions for a given day (i) as follows:

$$\widehat{\boldsymbol{x}}_i = \boldsymbol{x}_i + \mathbf{K}_i(\boldsymbol{y}_i - H_i\boldsymbol{x}_i), \tag{6}$$

where $\mathbf{K}$ is the Kalman gain defined by

$$\mathbf{K}_i = \mathbf{P}_i H_i^T \left(H_i \mathbf{P}_i H_i^T + \mathbf{R}_i\right)^{-1}, \tag{7}$$

Next, we applied the ratio of the a posteriori to a priori emissions and rerun the model. The major key point and difference between the Kalman filter and the Bayesian method are that the a priori covariance is not constant; that is, our level of understanding of uncertainty of emissions alters as we incorporate individual observations. It is expected that the errors of posteriori emissions continue to decrease after each iteration. In addition, when the number of observations is large, estimations of the covariance matrix of the posteriori emissions are likely to be overly optimistic (Jacob et al., 2016). Consequently, as time passes, this overconfidence in the priori values becomes too large, which in turn causes the inverse modeling system to become decoupled from the truth. To overcome this tendency, we determined a covariance inflation constant (λ) through trial and error. The schematic of the inversion is outlined in Figure 2.

It is worth noting that the assumption on the linear relationship between observations and emissions may not be entirely right in highly polluted regions (Souri et al., 2017). As sampling sizes of model and observation decrease over a polluted area, the relationship will deviate from a linear form to an exponential one. Here we made use of local gradients from DDM to linearize the nonlinear relationship. Given chemical feedbacks at such a high resolution, using a local gradient was preferable to a bulk ratio suggested by Martin et al. (2003). Nonetheless, we did not consider the second- or higher-order sensitivities to perform a nonlinear inverse modeling (e.g., the extended Kalman filter) which certainly requires a separate follow-up study.

3. Results and Discussion

3.1. GCAS Error Characterization

The major uncertainty in the NO_2 retrieval (40–60%) arises from the calculation of the AMF (Lorente et al., 2017). Thus, we examined the primary inputs and the vertical distribution of the SWs and SFs. The statistical distribution of the main inputs to the GCAS sampling is depicted in Figure 3a. Theoretically, a higher surface albedo results in a higher sensitivity of the sensor to NO_2 (i.e., larger SWs), attributed to a stronger reflection of solar radiance. The MODIS BRDF suggested a surface albedo in the HGB region of 0.04 ± 0.01, which was low because of abundant vegetation. We expected that this feature would have contributed to a lower AMF. Our tests using the LIDORT also suggested that the sensitivity of SWs to surface albedo was stronger over dark regions (not shown) (Boersma et al., 2004). One unintended consequence would have the amplification of the propagation of error of the albedo in the AMF. The viewing geometry of the GCAS sensor showed, on average, observations that were collected at 51° and 13° for solar and sensor zenith angles, respectively. Typically, for a high Solar Zenith Angles (SZA) range, the sensitivity of GCAS to NO_2 becomes lower/higher at the near surface/free troposphere. Solar radiation at higher SZA more aggressively scatter in the free atmosphere due to Rayleigh scattering. In response, radiation near the surface significantly attenuates.

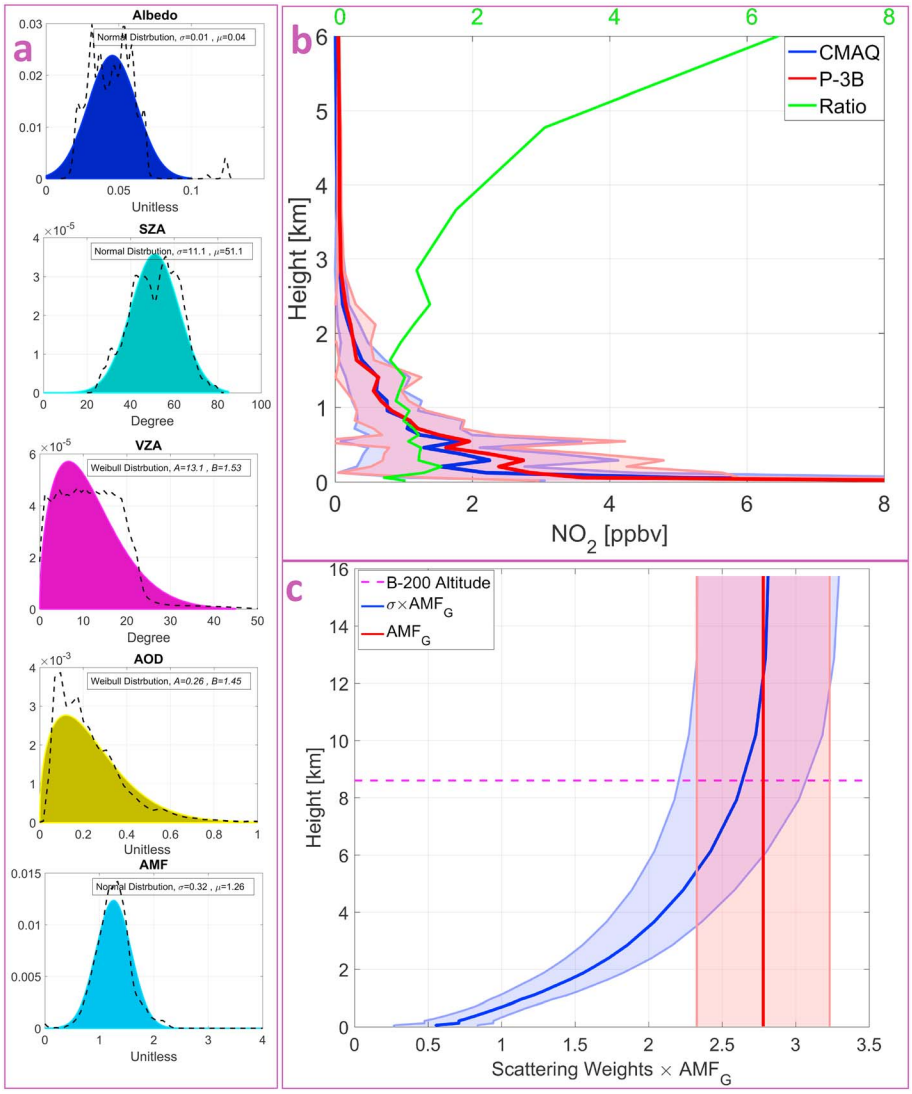

Figure 3. (a) The historgram of major inputs used in linearized discrete ordinate radiative transfer for estimating the scattering weights (black dashed line). The fitted distributions (colorful solid lines) are statistically significant according to the Kolmogorov-Smirnov test. (b) The priori NO_2 profile seen/simulated by P-3B/Community Multiscale Air Quality (CMAQ) that was used for estimating the shape factors. (c) The resulting averaged scattering weights multiplied by the geometric air mass factor (AMF_G), represented by the box AMF (blue line) and the corresponding standard deviation (blue shading). The AMF_G values and their standard deviation are represented by the red line and shading, respectively. AOD = aerosol optical depth; SZA = Solar Zenith Angle; VZA = Viewing Zenith Angle.

The AMF dependence on aerosols is complicated by variation in the optical properties of individual aerosol types. Depending on the refractive indices, size distributions, and hygroscopic growth rates of each aerosol type, we estimated the AOD at 432 nm from the CMAQ using Flexible Aerosol Optical Depth, described in Curci et al. (2015). We found an average AOD of 0.26 ± 0.2 at the GCAS scanlines. The magnitude of simulated AOD aligned with that of AErosol RObotic NETwork (AERONET) atop the University of Houston Moody Tower (AOD = 0.20) (not shown). Our case study showed that the low amount of AOD did not result in a considerable impact on AMF (< 5–10%) on average but might be crucial for specific episodes.

Because of the relatively large impact of SFs on the AMF, we need to investigate whether or not the CMAQ predictions for the NO_2 profiles are reasonable. To answer this question, we compared our model results with 10 day P-3B NO_2 measurements (Figure 3b). While our model overpredicted NO_2 near the surface layer, it persistently underpredicted NO_2 mixing ratios in the free troposphere up to a factor of 6. The reason for this

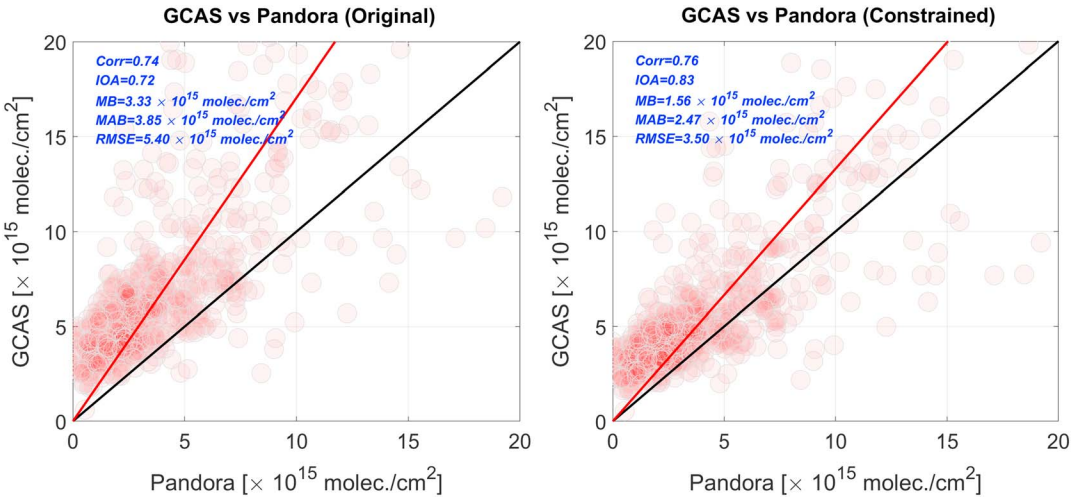

Figure 4. The scatter plot of the Geostationary Coastal and Air Pollution Events Airborne Simulator (GCAS) vertical column densities versus the Pandora Spectrometer Instrument vertical column densities (before and after constraining the surface albedo). For a direct comparison, we subtracted the aircraft columns modeled above from the Pandora Spectrometer Instrument total columns. RMSE = root-mean-square error; Corr: correlation; IOA: Index of Agreement; MB: Mean Bias; MAB: Mean Absolute Bias.

discrepancy was unclear, but we could attribute it to the uncertainties associated with the lightning scheme, aviation emissions, chemical processes or vertical mixing mechanisms. Although the large underprediction of NO_2 in the free troposphere may appear to be unimportant, the large sensitivity of the GCAS to NO_2 and the thicker vertical layers (i.e., larger $d\sigma$) at these levels imply that it is actually important. Thus, we increased the accuracy of the priori NO_2 profile using P-3B observations by applying the ratio of observations to the model.

Using the RTM, we further calculate the SWs on the altitude coordinates with CMAQ vertical layers at a vertical resolution of 50 m to 2 km. Then we multiplied the values by the AMF_G to estimate the box AMF, shown in Figure 3c, and found that the SWs increased exponentially with altitude. This is because of the fact that radiation weakens the deeper it travels into the atmosphere. Hence, the GCAS sensor was more sensitive to NO_2 concentrations in the upper atmosphere. The standard deviations of the SWs increased in the same manner, resulting from a greater sensitivity of the SW to inputs used in the RTM at higher altitudes (Lamsal et al., 2017). It is highly unlikely, however, that the sensitivity of the sensor to the gas is greater than to a scatter-free atmosphere, indicating that the box AMF must roughly converge to AMF_G (2.67 ± 0.48) in the upper troposphere, where scattering is insignificant. This condition is highly consistent with the findings of this study. The averaged AMF estimated from the SWs, and the SFs is 1.26 ± 0.32 for all GCAS samples (Figure 3a).

To characterize the error of GCAS NO_2 VCDs, we used the PSI measurements at 11 stations in our domain. Owing to the fact that NO_2 concentrations vary quickly by time, we collected only those measurements that were coincident with the GCAS observations within a small radius (<2 km) and short period (<36 s). We removed the above aircraft NO_2 columns (~2.8–3.1 × 10^{15} molecules cm^{-2}) from the PSI total columns based on the GEOS-Chem model (Bey et al., 2001) to perform an apples-to-apples comparison and found a 0.74 correlation (r) between the two data sets for all days (left panel in Figure 4). On more than 6 days, the GCAS observations showed a striking correspondence to those of PSI ($r > 0.85$) (not shown). Results revealed that the GCAS VCDs were overestimated (70%) with a bias of 3.33 × 10^{15} molecules cm^{-2}. Some inconsistencies between the two data sets might have originated from (i) the different air masses used by the two sensors, (ii) the uncertainty of the global model used in estimating the above aircraft NO_2 column, and (iii) errors in the retrieval process and the AMF calculation.

The overestimation of the GCAS VCDs was problematic. It could have been propagated in the inversion, inducing bias in the top-down estimation later. Fortunately, the PSI observations enabled us to mitigate this problem. Such an overestimation might be removed by simply scaling all GCAS VCDs with respect to the factor of overestimation, indicating that we would consider the below aircraft VCDs from PSI being free from any types of error, which is unrealistic. A sounder way would be to constrain the major source of bias. Among the AMF

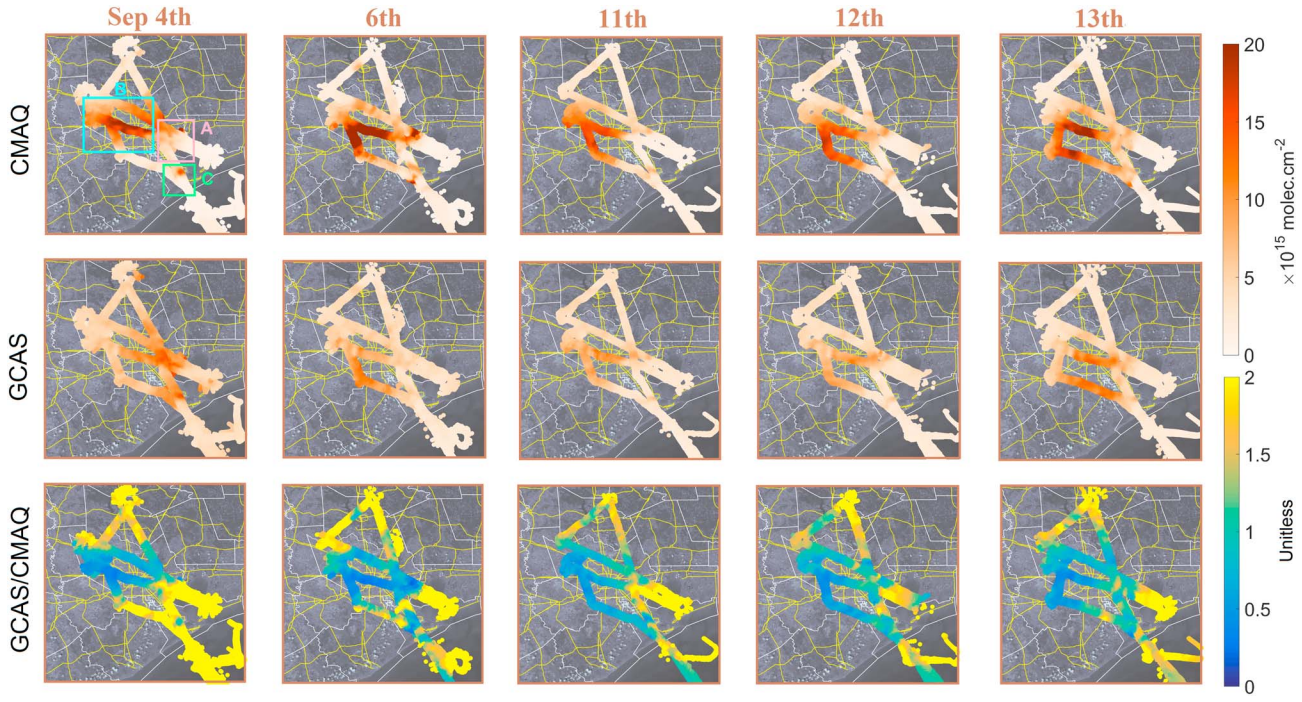

Figure 5. The spatial distribution of vertical NO_2 columns observed by Community Multiscale Air Quality (CMAQ) (first row) and Geostationary Coastal and Air Pollution Events Airborne Simulator (GCAS) (second row), the ratio of GCAS to CMAQ (third row), coregistered in time and space. The GCAS vertical column densities are based on the air mass factors estimated in this study. Regions A, B, and C denote the Houston Shipping Channel, the Houston metropolitan area, and Texas City, respectively. The overprediction of CMAQ over NO_x hot spots is observed.

inputs, we believed that the absolute amount of the MODIS BRDF was the major cause of the overestimation, as former studies found this quantity highly uncertain (particularly at shorter wavelengths) (Wang et al., 2010), with an underestimation of up to 0.02 at 0.3–5 μm channels (Salomon et al., 2006). Under the assumption that the uncertainty of PSI is 25% and that of the MODIS BRDF observations is 50%, we constrained the albedo using Bayesian inversion (equation (5)) in conjunction with LIDORT as a forward model (i.e., Jacobian matrix). Here the unknown was the average of all surface albedo (one value), and observations were all available PSI measurements. For this optimization, we assumed no temporal or spatial dependence. We found the constrained surface albedo to be 0.063 ± 0.007, which was 0.023 larger than the original albedo. The resultant AMF increased to 1.54 ± 0.50, reducing the overestimation of GCAS by ~23% (right panel of Figure 4). Interestingly, the constrained AMF did not mitigate the overestimation uniformly across all observations because the AMF was more sensitive to very dark surfaces (where we had too low AMF and, thus, too high VCDs). From the root-mean-square error value obtained from this comparison, we set the uncertainty of the GCAS observations for the inversion to 3.5×10^{15} molecules cm^{-2} (0.13 DU out of a typical value of 1 DU or 2.69×10^{16} molecules cm^{-2}). We found an acceptable agreement (within 7% difference) between the estimated AMF from our study to the AMF calculated for Geostationary Trace Gas and Aerosol Sensor Optimization sensor (1.45 ± 0.49) flying over the area during the same campaign (Nowlan et al., 2016).

3.2. Top-Down Emissions Using GCAS VCDs

3.2.1. GCAS Versus CMAQ

Prior to constraining the anthropogenic NO_x emissions using the GCAS NO_2 VCDs, we believed that compiling an overall picture of the extent to which the magnitudes and the spatial patterns of the CMAQ NO_2 VCDs differed from those of GCAS could be valuable. Figures 5 and 6 demonstrate the spatial distribution of NO_2 VCDs from CMAQ and GCAS over the HGB region. Both data sets showed high NO_2 concentrations in the center of Houston, indicating predominant anthropogenic NO_x emissions, particularly from mobile sources. Three major areas that contributed the most to NO_2 concentrations were the Houston Ship Channel (HSC(54 t/d, region A), the Houston metropolitan area (145 t/d, region B), and Texas City (17 t/d, region C). Correlations between the CMAQ and GCAS VCDs, along with other statistics, are listed in Table 1. A strong

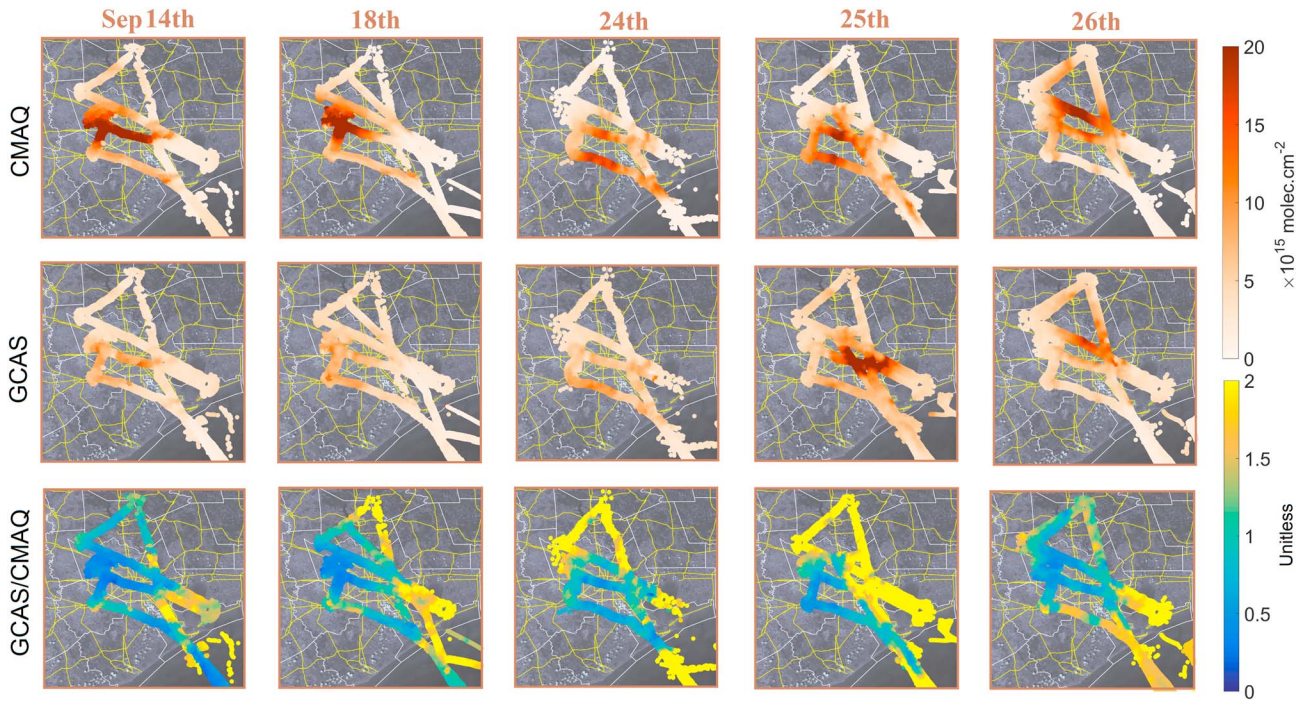

Figure 6. Same as Figure 5. A large underprediction of the model likely resulting from unexpected local sources from region A was revealed on 25 September.

correlation between the two data sets (0.70 ± 0.18) indicated that the transport and location of NO_x sources were relatively reasonable. From observations, the ratios of the GCAS NO_2 VCDs to those of CMAQ were 0.74 ± 0.22 over high NO_x regions (ENO_x > 0.2 mol/s), possibly reflecting the well-documented overprediction of NO_x emissions (e.g., Souri et al., 2016; Travis et al., 2016).

We noted that the CMAQ, however, largely underpredicted NO_2 columns on 25 September by a factor of 1.3. These unprecedented high NO_2 concentrations over the HSC have been a focus of debate (Pan, Choi, Jeon, et al., 2017; Souri et al., 2016). One potential reason for the lack of agreement between the model and the observations is the rapid local NO_x production from point sources in the HSC region. Souri et al. (2016) found a sharp reduction in the P-3B NO_y/NO_x ratios, which provide some insights into the photochemical aging processes, suggesting that the abnormally high NO_x concentrations originated from the local sources. A second potential reason for the discrepancy is the inability of the weather model to simulate wind fields that promote the convergence of pollutants over the region (Pan, Choi, Jeon, et al., 2017). Pan, Choi, Jeon, et al. (2017) substantially altered the wind pattern to reproduce a relatively stagnant condition during early morning and the convergence at noon. Although they managed to partly mitigate the bias of model in simulating NO_x concentrations, they demonstrated that the transport could not fully resolve the issue. Since it was implausible that transport was the sole reason for such an unusually high observed NO concentration (>100 ppbv) over the surface (not shown) and the NO_2 column ($>30 \times 10^{15}$ molecules cm^{-2}), we assumed that the discrepancy between the model predictions and observations resulted from bias in the local NO_x

Table 1
The Statistics Computed From the Comparison Between the CMAQ and GCAS NO_2 VCDs During 2013 September

Metrics	4th	6th	11th	12th	13th	14th	18th	24th	25th	26th
Correlation	0.41	0.69	0.82	0.81	0.73	0.78	0.77	0.84	0.34	0.80
Mean bias[a]	−0.29	2.72	1.52	1.55	1.41	3.80	3.10	1.42	−2.19	1.37
RMSE	4.93	6.26	3.42	3.45	3.78	6.56	6.02	3.19	5.88	3.64
Ratio—high[b]	0.81	0.57	0.76	0.73	0.74	0.49	0.56	0.78	1.28	0.73

Note. CMAQ = Community Multiscale Air Quality; GCAS = Geostationary Coastal and Air Pollution Events Airborne Simulator; VCDs = vertical column densities; RMSE = root-mean-square error. The unit for Mean bias and RMSE is $\times 10^{15}$ molecules/cm^2.
[a]The bias is the model minus observation. [b]Defined as the ratio of GCAS to CMAQ in high NO_x regions (ENO_x > 0.2 mol/s).

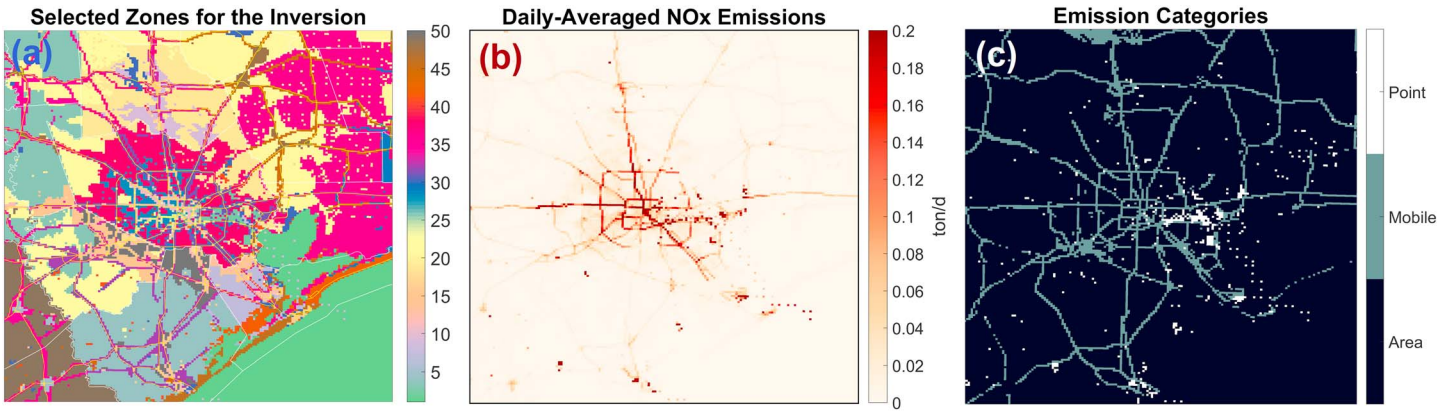

Figure 7. (a) The selected zones for aggregating emissions (i.e., state vectors) determined by the Gaussian mixture model method. The purpose of aggregating emissions is to compensate for the insufficient amount of information in data with respect to the unknowns (i.e., emissions). (b) The daily-averaged NO_x emissions in September 2013. (c) The dominant emissions sectors for each grid cell.

emissions. Fortunately, GCAS offered a unique opportunity to constrain emissions for this specific event, which was lacking in former studies using satellites (e.g., Souri et al., 2016).

3.2.2. Original Versus Updated Emissions

As mentioned earlier, this study examined the feasibility of GCAS NO_2 VCDs using the Kalman filter to constrain anthropogenic emissions. A major challenge for this task was the spatial coverage of GCAS, which may not have been sufficient to resolve emissions in the native resolution, known as the smoothing error. A solution to the above issue is to reduce the dimension of the state vectors (emissions) by aggregating emissions. Nevertheless, clustering emissions could also introduce another type of uncertainty called the "aggregation error." We chose optimal aggregated zones by running the inversion multiple times, each with a certain selection of state vectors (Turner & Jacob, 2015). This study used the GMM method to cluster emissions into certain zones that shared roughly similar features. We found 50 zones resulting in the minimum value of the sum of the aggregation and smoothing errors among 3 to 60 clusters, shown in Figure 7a. The spatial distribution of emissions and the corresponding dominant categories are, respectively, depicted in Figures 7b and 7c. Figures 7b and 7c demonstrated that the classification method was skillful not only at separating the emissions by their magnitude and category but also by differentiating their geographic locations.

Figures 8 and 9 present the comparison of the CMAQ modeling results and independent surface measurements before and after the inversion as well as the geographic distribution of differences between the a priori and a posteriori NO_x emissions. The time period for this figure is 8 a.m. to 4 p.m. The results in Figure 8 (4 to 13 September) show that more than 306 k qualified observations were utilized, which constrained the emissions. Compared to the Continuous Ambient Monitoring Stations data, the a priori emissions data yielded a consistent spatial distribution of surface NO_2 ($r = 0.78 \pm 0.08$). However, the overall a priori overestimated emissions resulted in a bias of 0.96 ± 0.76 ppbv. The ratio of GCAS to CMAQ suggested that the majority of the overprediction of the model occurred in the Houston metropolitan area (Souri et al., 2016), which was also observed in surface observations. After the inversion, a posteriori emissions suggested a 4–40% reduction in emissions. The optimization, however, increased emissions (6–152%) over rural/suburban regions, where the model typically tended to underpredict NO_2 columns. It is reassuring to see that the magnitude of reduction in the NO_x emissions over polluted areas aligned with the bias of the model. To validate the results of the inversion, we compared the model output with a posteriori emissions to the monitoring data and found a 42–123% reduction in the mean bias, except for the results on 11 and 12 September. Although the inversion contributed to reducing emissions slightly, counterbalancing the positive bias of model for these specific days, the reduction was overshadowed by enhancements in other regions.

Although the a posteriori covariance remained roughly unchanged because of the low number of observations for rural and suburban regions, it decreased by 2 orders of magnitude for urban areas. For these regions, we found that the inflation factor (λ) should be set at 50 since (i) the large number of observations generally

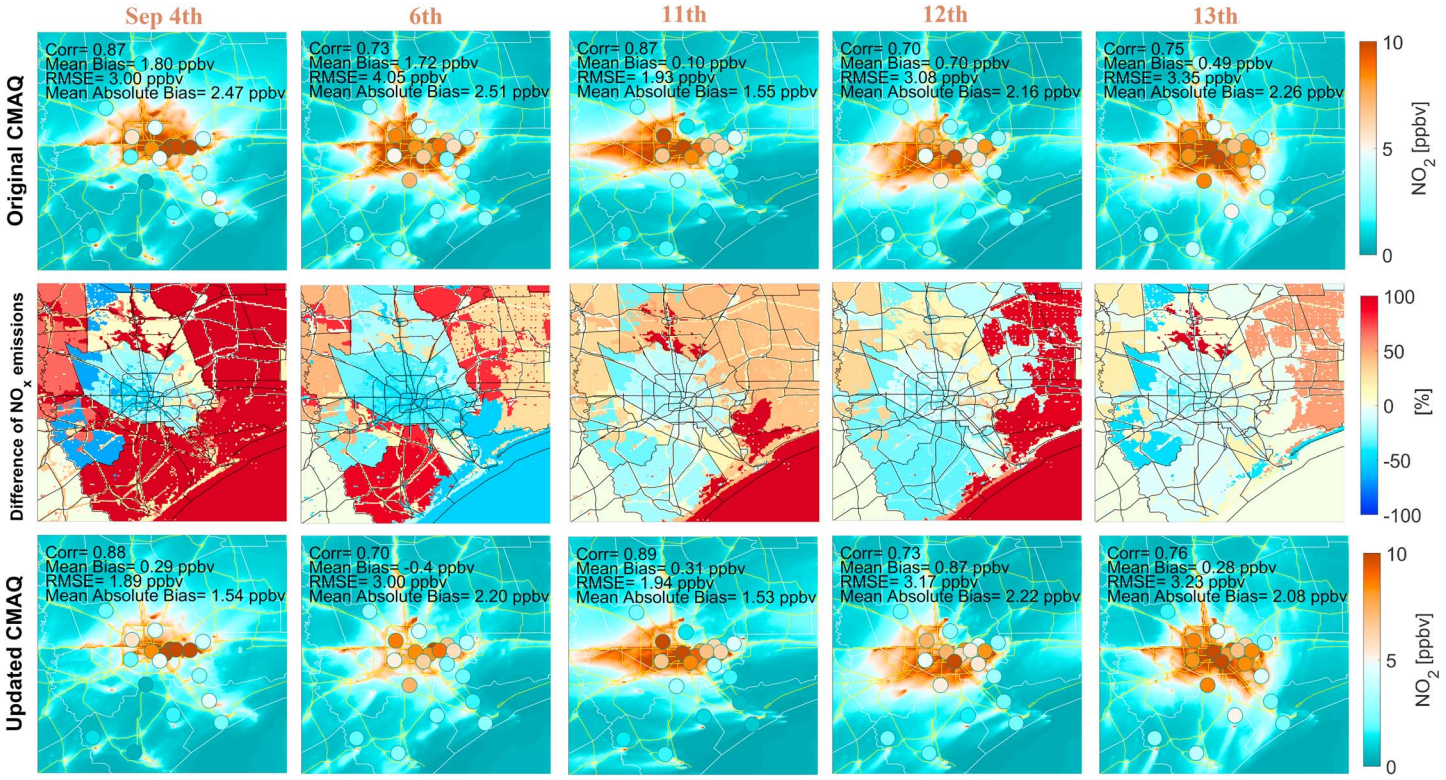

Figure 8. Changes in simulating the surface NO_2 concentration at 8 a.m. to 4 p.m. by constraining anthropogenic emissions using Geostationary Coastal and Air Pollution Events Airborne Simulator NO_2 vertical column densities. First row: simulated surface NO_2 concentrations contrasted with Continuous Ambient Monitoring Stations observations. Second row: the percentage difference between the a posteriori and a priori emissions in 50 clusters determined by the Gaussian mixture model. Third row: the same as the first row but after the inversion. CMAQ = Community Multiscale Air Quality.

resulted in an overinterpretation of the a posteriori errors (Jacob et al., 2016) and (ii) the short lifetime of NO_x downplayed the impact of updated (today's) emissions for more accurate simulation in the future.

Similar to the previous figure, Figure 9 (14 to 26 September) shows that the modeled NO_2 was overpredicted in urban areas (0.63 ppbv), except for the 25 September case. The inversion suggested a 3–51% reduction in anthropogenic NO_x emissions in the urban areas, representing a partial mitigation; the reduction might have been overshadowed by enhancements in nonurban regions. A more detailed discussion on this limitation will be provided later. Interestingly, although the performance of the model was inferior at simulating surface NO_2 on 24 September ($r = 0.14$), it coincided well with GCAS VCDs ($r = 0.84$), suggesting that surface concentration may not always be entirely related to the column.

The 25 September event was of particular interest because of the abnormally high NO_2 concentrations that led to the strong degradation of air quality. From the comparison of surface measurements to the model output, we observed a large negative bias (−4.2 ppbv) and relatively poorer correlation ($r = 0.50$). The mean bias for wind speed during this episode was low (0.5 m s^{-1}) (Pan, Choi, Jeon, et al., 2017), indicating that the emissions may have been so inaccurate that the model was not able to reproduce NO_2 concentrations. Interestingly, the sound inversion method and the high-quality GCAS observations counterbalanced the bias (1.03 ppbv) by increasing the amplitude of NO_x emissions (94%) in the urban areas. However, the improvement in the correlation was insignificant, mostly the result of the low spatial coverage of GCAS observations. If the number of aggregated state vectors had been enhanced to constrain emissions in a more spatially finer manner, such data gaps over several parts of the domain would have inevitably led to an underconstrained problem.

Overall, except the 25 September event, we observed that the inversion consistently decreased NO_x emissions in highly polluted areas. The magnitudes of reduction were in line with the bias of model in respect with both the surface and the GCAS observations. Some variations associated with the daily emissions were

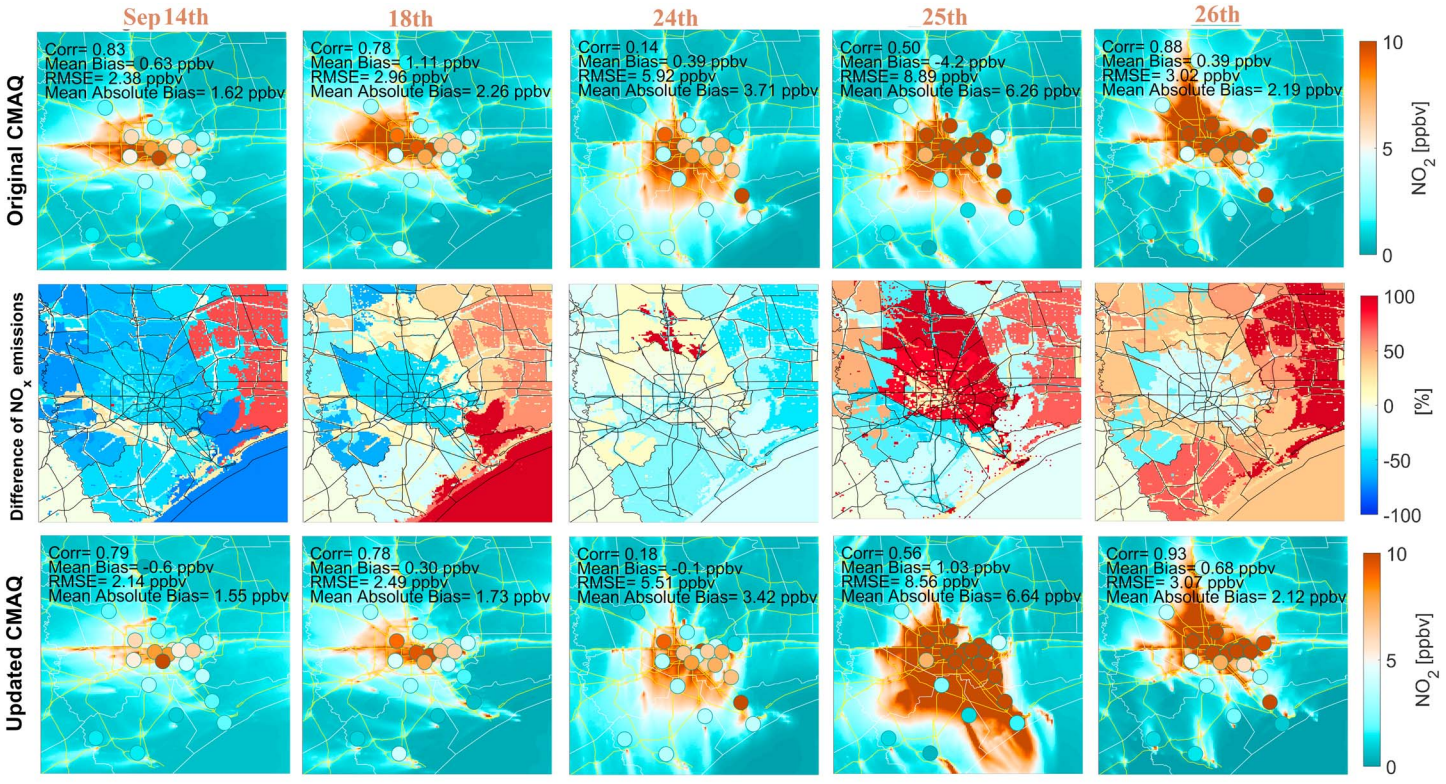

Figure 9. Same as Figure 8 but for the 14 to 26 September time period.

attributed to the industrial sectors (Nam et al., 2008). On the other hand, the resultant changes in the posteriori emissions varied dramatically day by day in suburban and rural regions which could be attributed to the facts that (i) the number of GCAS samples to the size of the nonurban zones was significantly low, (ii) a weaker NO_2 signal in less polluted regions contributed to less certain observations which were not fully characterized in our study, (iii) the impact of uncertainties associated with the transport on the inversion was more substantial at those regions, and (iv) a lack of a regular monitoring system resulted in large uncertainty of the area sector which dominantly covered the nonurban regions.

We previously observed that the agreement between optimized emissions and the model bias in a specific region decreased as background NO_2 from other areas increased. The best example of this phenomenon occurred on 25 September. The CMAQ simulation with the a priori emissions suggested a considerable underprediction of NO_x emissions in the northern/northeastern parts of Houston but overpredictions in the southern areas. Given the high quality of GCAS observations, the a posteriori emissions exhibited a similar trend. Nevertheless, because of transport, the significant enhancements in NO_x emissions in the northern parts eventually affected the southern parts. The role of transport in misalignment between observations and emissions is a major challenge in inverse modeling studies at regional scales. A sound way of tackling the above issue is to explicitly quantify the relationship between the NO_2 concentration for a given region (i.e., receptor) and emissions in the remaining zones (i.e., sources). As a result, we will take the positive bias of the model (with respect to observations) in southern Houston into account while constraining the emissions in the northern parts. As analytically calculating the derivative of a receptor to several sources given chemical feedback is a daunting task, the development/update of adjoint regional models that numerically address this task will be needed in the future.

4. Summary

Several studies have shown the capability of spaceborne remote sensing satellites to monitor emissions. However, instrumental degradation of current sensors and their relatively insufficient spatial and temporal

resolutions has introduced a burden to constrain emissions at fine scales. To address this gap, we presented, for the first time, an application of NO_2 columns from the Airborne Compact Atmospheric Mapper (GCAS) onboard the NASA B200 aircraft for constraining anthropogenic NO_x ($NO + NO_2$) emissions during the DISCOVER-AQ Texas campaign. Our first attempt to incorporate the observations into an analytical inversion was to convert the NO_2 SCD into vertical values. To this end, we estimated AMFs from a radiative transfer model with (i) a priori NO_2 profiles from a high-resolution CMAQ model (1×1 km^2) constrained by P-3B NO_2 measurements, (ii) a simulated absorption optical depth based on Mie's theory from the CMAQ, and (iii) high-resolution MODIS surface BRDFs. The averaged AMF was 1.26 ± 0.27 for all of the GCAS samples. We converted more than 615 k qualified pixels into vertical columns, validated them against surface PSI measurements, and found a strong correlation between the two data sets ($r = 0.74$). However, we found overestimates of GCAS VCDs (~70%). To address this issue, we constrained the surface albedo using PSI observations via Bayesian inversion, leading to an increase in the surface albedo of 0.023, which strongly correlated with the bias found by Salomon et al. (2006). The constrained surface albedo considerably reduced the discrepancy between the observations. PSI measurements suggested an uncertainty of 3.5×10^{15} molecules cm^{-2} (0.13 DU out of a typical value of 1 DU or 2.69×10^{16} molecules cm^{-2}) for the GCAS NO_2 VCDs.

To constrain emissions, we used an inversion method based on the Kalman filter, and to explicitly find the first derivative of observations to emissions (i.e., Jacobian matrix), we used CMAQ-DDM (1×1 km^2). The high quality of GCAS observations enabled us to perform a day-to-day inversion during September 2013. We found that with the accuracy and the number of GCAS observations, we were able to partially reduce the well-documented overprediction of the model at reproducing surface NO_2 on regular days; the constrained emissions suggested an overall 2 to 50% reduction in anthropogenic NO_x emissions in polluted areas. On the other hand, we observed a significant underprediction of the model at simulating surface and columnar NO_2 concentrations on 25 September. Fortunately, GCAS observations, coupled with the sound inversion method, mitigated the underprediction of the model by enhancing emissions by 94%, which reduced the model bias by 123% (from −4.2 to 1.03 ppbv). Improving the accuracy of emissions for this type of event ensures that next-generation satellites (with better spatial and temporal resolutions) should have a unique capability to detect and constrain emissions anomalies.

To enhance the capability of quantifying emissions on a regional scale, previous studies should have oversampled spaceborne remote sensing observations, and if they had done so, they may not have captured fine variations in emissions. With high-quality airborne observations, we were able to narrow down the inversion window from a year/month to a day. However, we are aware of the limitations of our work: (i) the airborne observations had a low spatial coverage and (ii) we did not account for the interconnection of aggregated state vectors. Thus, transport partly have led to the misalignment in emissions and observations, and (iii) the uncertainties of winds simulation were well within the ranges suggested by Liu et al. (2017), yet the transport error was likely to influence the inversion. The first limitation could be addressed by integrating qualified pixels from satellites and the second by numerically solving optimization that requires an adjoint model.

Acknowledgments

Amir H. Souri acknowledges support by the UH Earth and Atmospheric Sciences Department Research Grant, the National Strategic Project-Fine particle of the National Research Foundation of Korea (NRF) funded by the Ministry of Science and ICT (MSIT), the Ministry of Environment (ME), and the Ministry of Health and Welfare (MOHW) (NRF-2017M3D8A1092022). We express our sincere appreciation to Robert Spurr for providing the LIDORT package and James H. Flynn for AOD measurements from AERONET. The authors also wish to recognize useful suggestions by Wonbae Jeon and Randall Martin. The model and observation data and the codes used for creating the figures or conducting the models will be made available from the corresponding author upon request. A. H. S. designed the research, analyzed the data, conducted CMAQ-DDM, estimated AMF, carried out the inverse modeling, produced all of the figures, and wrote the manuscript. Y. C., J. L., and C. R. N. conceived and guided the interpretation. S. P. provided the emissions using SMOKE and conducted the WRF. G. C. implemented FlexAOD for CMAQ. C. R. N. applied the spectral fit algorithm to retrieve the slant columns. S. J. Z. and M. K. collected the GCAS observations. J. H. provided the PSI observations. A. J. W. provided the P-3B observations. All authors contributed to discussions and edited the manuscript.

References

Bey, I., Jacob, D. J., Yantosca, R. M., Logan, J. A., Field, B. D., Fiore, A. M., et al. (2001). Global modeling of tropospheric chemistry with assimilated meteorology: Model description and evaluation. *Journal of Geophysical Research*, *106*(D19), 23,073–23,095. https://doi.org/10.1029/2001JD000807

Bishop, C. M. (2007). *Pattern recognition and machine learning* (1st ed.). New York: Springer.

Boersma, K. F., Eskes, H. J., & Brinksma, E. J. (2004). Error analysis for tropospheric NO_2 retrieval from space. *Journal of Geophysical Research*, *109*, D04311. https://doi.org/10.1029/2003JD003962

Brewer, A. W., McElroy, C. T., & Kerr, J. B. (1973). Nitrogen dioxide concentrations in the atmosphere. *Nature*, *246*(5429), 129–133. https://doi.org/10.1038/246129a0

Byun, D., & Schere, K. L. (2006). Review of the governing equations, computational algorithms, and other components of the models-3 Community Multiscale Air Quality (CMAQ) modeling system. *Applied Mechanics Reviews*, *59*(2), 51–77. https://doi.org/10.1115/1.2128636

Chai, T., Carmichael, G. R., Tang, Y., Sandu, A., Heckel, A., Richter, A., & Burrows, J. P. (2009). Regional NO_x emission inversion through a four-dimensional variational approach using SCIAMACHY tropospheric NO_2 column observations. *Atmospheric Environment*, *43*(32), 5046–5055. https://doi.org/10.1016/j.atmosenv.2009.06.052

Chance, K. (1998). Analysis of BrO measurements from the Global Ozone Monitoring Experiment. *Geophysical Research Letters*, *25*(17), 3335–3338. https://doi.org/10.1029/98GL52359

Cohan, D. S., Hakami, A., Hu, Y., & Russell, A. G. (2005). Nonlinear response of ozone to emissions: Source apportionment and sensitivity analysis. *Environmental Science & Technology*, *39*(17), 6739–6748. https://doi.org/10.1021/es048664m

Curci, G., Hogrefe, C., Bianconi, R., Im, U., Balzarini, A., Baró, R., et al. (2015). Uncertainties of simulated aerosol optical properties induced by assumptions on aerosol physical and chemical properties: An AQMEII-2 perspective. *Atmospheric Environment*, *115*, 541–552. https://doi.org/10.1016/j.atmosenv.2014.09.009

Ding, J., Miyazaki, K., Mijling, B., Kurokawa, J. I., Cho, S., Janssens-Maenhout, G., et al. (2017). Intercomparison of NO_x emission inventories over East Asia. *Atmospheric Chemistry and Physics*, *17*(16), 10,125–10,141. https://doi.org/10.5194/acp-17-10125-2017

Herman, J., Cede, A., Spinei, E., Mount, G., Tzortziou, M., & Abuhassan, N. (2009). NO_2 column amounts from ground-based Pandora and MFDOAS spectrometers using the direct-Sun DOAS technique: Intercomparisons and application to OMI validation. *Journal of Geophysical Research*, *114*, D13307. https://doi.org/10.1029/2009JD011848

Huang, M., Bowman, K. W., Carmichael, G. R., Chai, T., Pierce, R. B., Worden, J. R., et al. (2014). Changes in nitrogen oxides emissions in California during 2005–2010 indicated from top-down and bottom-up emission estimates. *Journal of Geophysical Research: Atmospheres*, *119*, 12,928–12,952. https://doi.org/10.1002/2014JD022268

Jacob, D. J., Turner, A. J., Maasakkers, J. D., Sheng, J., Sun, K., Liu, X., et al. (2016). Satellite observations of atmospheric methane and their value for quantifying methane emissions. *Atmospheric Chemistry and Physics*, *16*(22), 14,371–14,396. https://doi.org/10.5194/acp-16-14371-2016

Jaeglé, L., Steinberger, L., Martin, R. V., & Chance, K. (2005). Global partitioning of NO_x sources using satellite observations: Relative roles of fossil fuel combustion, biomass burning and soil emissions. *Faraday Discussions*, *130*, 407–423. https://doi.org/10.1039/b502128f

Kowalewski, M. G., & Janz, S. J. (2014). Remote sensing capabilities of the GEO-CAPE airborne simulator, Proc. SPIE 9218, Earth Observing Systems XIX, 92181I.

Lamsal, L. N., Janz, S. J., Krotkov, N. A., Pickering, K. E., Spurr, R. J. D., Kowalewski, M. G., et al. (2017). High-resolution NO_2 observations from the Airborne Compact Atmospheric Mapper: Retrieval and validation. *Journal of Geophysical Research: Atmospheres*, *122*, 1953–1970. https://doi.org/10.1002/2016JD025483

Lamsal, L. N., Martin, R. V., Van Donkelaar, A., Steinbacher, M., Celarier, E. A., Bucsela, E., et al. (2008). Ground-level nitrogen dioxide concentrations inferred from the satellite-borne Ozone Monitoring Instrument. *Journal of Geophysical Research*, *113*, D16308. https://doi.org/10.1029/2007JD009235

Liu, X., Mizzi, A. P., Anderson, J. L., Fung, I. Y., & Cohen, R. C. (2017). Assimilation of satellite NO_2 observations at high spatial resolution using OSSEs. *Atmospheric Chemistry and Physics*, *17*(11), 7067–7081.

Lorente, A., Boersma, K. F., Yu, H., Dörner, S., Hilboll, A., Richter, A., et al. (2017). Structural uncertainty in air mass factor calculation for NO_2 and HCHO satellite retrievals. *Atmospheric Measurement Techniques*, *10*(3), 759–782.

Martin, R. V., Jacob, D. J., Chance, K., Kurosu, T. P., Palmer, P. I., & Evans, M. J. (2003). Global inventory of nitrogen oxide emissions constrained by space-based observations of NO_2 columns. *Journal of Geophysical Research*, *108*(D17), 4537. https://doi.org/10.1029/2003JD003453

Mijling, B., Ding, J., Koukouli, M. E., Liu, F., Li, Q., Mao, H., & Theys, N. (2017). Cleaning up the air: Effectiveness of air quality policy for SO_2 and NO_x emissions in China. *Atmospheric Chemistry and Physics*, *17*(3), 1775–1789.

Mijling, B., & van der A, R. J. (2012). Using daily satellite observations to estimate emissions of short-lived air pollutants on a mesoscopic scale. *Journal of Geophysical Research*, *117*, D17302. https://doi.org/10.1029/2012JD017817

Miyazaki, K., Eskes, H., Sudo, K., Boersma, K. F., Bowman, K., & Kanaya, Y. (2017). Decadal changes in global surface NO_x emissions from multi-constituent satellite data assimilation. *Atmospheric Chemistry and Physics*, *17*(2), 807–837.

Miyazaki, K., Eskes, H. J., Sudo, K., Takigawa, M., Van Weele, M., & Boersma, K. F. (2012). Simultaneous assimilation of satellite NO_2, O_3, CO, and HNO_3 data for the analysis of tropospheric chemical composition and emissions. *Atmospheric Chemistry and Physics*, *12*(20), 9545–9579. https://doi.org/10.5194/acp-12-9545-2012

Nam, J., Webster, M., Kimura, Y., Jeffries, H., Vizuete, W., & Allen, D. T. (2008). Reductions in ozone concentrations due to controls on variability in industrial flare emissions in Houston, Texas. *Atmospheric Environment*, *42*(18), 4198–4211. https://doi.org/10.1016/j.atmosenv.2008.01.035

Nowlan, C. R., Liu, X., Leitch, J. W., Chance, K., González Abad, G., Liu, C., et al. (2016). Nitrogen dioxide observations from the Geostationary Trace gas and Aerosol Sensor Optimization (GeoTASO) airborne instrument: Retrieval algorithm and measurements during DISCOVER-AQ Texas 2013. *Atmospheric Measurement Techniques*, *9*(6), 2647–2668. https://doi.org/10.5194/amt-9-2647-2016

Palmer, P. I., Jacob, D. J., Chance, K., Martin, R. V., Spurr, R. J. D., Kurosu, T. P., et al. (2001). Air mass factor formulation for spectroscopic measurements from satellites: Application to formaldehyde retrievals from the Global Ozone Monitoring Experiment. *Journal of Geophysical Research*, *106*(D13), 14,539–14,550. https://doi.org/10.1029/2000JD900772

Pan, S., Choi, Y., Jeon, W., Roy, A., Westenbarger, D. A., & Kim, H. C. (2017). Impact of high-resolution sea surface temperature, emission spikes and wind on simulated surface ozone in Houston, Texas during a high ozone episode. *Atmospheric Environment*, *152*, 362–376. https://doi.org/10.1016/j.atmosenv.2016.12.030

Pan, S., Choi, Y., Roy, A., & Jeon, W. (2017). Allocating emissions to 4 km and 1 km horizontal spatial resolutions and its impact on simulated NO_x and O_3 in Houston, TX. *Atmospheric Environment*, *164*, 398–415. https://doi.org/10.1016/j.atmosenv.2017.06.026

Qu, Z., Henze, D. K., Capps, S. L., Wang, Y., Xu, X., Wang, J., & Keller, M. (2017). Monthly top-down NO_x emissions for China (2005–2012): A hybrid inversion method and trend analysis. *Journal of Geophysical Research: Atmospheres*, *122*, 4600–4625. https://doi.org/10.1002/2016JD025852

Ridley, B. A., & Grahek, F. E. (1990). A small, low flow, high sensitivity reaction vessel for NO chemiluminescence detectors. *Journal of Atmospheric and Oceanic Technology*, *7*(2), 307–311. https://doi.org/10.1175/1520-0426(1990)007%3C0307:ASLFHS%3E2.0.CO;2

Ridley, B., Ott, L., Pickering, K. E., Emmons, L., Montzka, D. D., Weinheimer, A., et al. (2004). Florida thunderstorms: A faucet of reactive nitrogen to the upper troposphere. *Journal of Geophysical Research*, *109*, D17305. https://doi.org/10.1029/2004JD004769

Rodgers, C. D. (2000). *Inverse methods for atmospheric sounding: Theory and practice* (Vol. 2). World Scientific. https://doi.org/10.1142/3171

Salomon, J. G., Schaaf, C. B., Strahler, A. H., Gao, F., & Jin, Y. (2006). Validation of the MODIS bidirectional reflectance distribution function and albedo retrievals using combined observations from the aqua and terra platforms. *IEEE Transactions on Geoscience and Remote Sensing*, *44*(6), 1555–1565. https://doi.org/10.1109/TGRS.2006.871564

Skamarock, W. C., & Klemp, J. B. (2008). A time-split nonhydrostatic atmospheric model for weather research and forecasting applications. *Journal of Computational Physics*, *227*(7), 3465–3485. https://doi.org/10.1016/j.jcp.2007.01.037

Souri, A. H., Choi, Y., Jeon, W., Li, X., Pan, S., Diao, L., & Westenbarger, D. A. (2016). Constraining NO_x emissions using satellite NO2 measurements during 2013 DISCOVER-AQ Texas campaign. *Atmospheric Environment*, *131*, 371–381. https://doi.org/10.1016/j.atmosenv.2016.02.020

Souri, A. H., Choi, Y., Jeon, W., Woo, J.-H., Zhang, Q., & Kurokawa, J.-i. (2017). Remote sensing evidence of decadal changes in major tropospheric ozone precursors over East Asia. *Journal of Geophysical Research: Atmospheres*, *122*, 2474–2492. https://doi.org/10.1002/2016JD025663

Spurr, R. (2008). LIDORT and VLIDORT: Linearized pseudo-spherical scalar and vector discrete ordinate radiative transfer models for use in remote sensing retrieval problems. In *Light scattering reviews 3* (pp. 229–275). Berlin, Heidelberg: Springer. https://doi.org/10.1007/978-3-540-48546-9_7

Travis, K. R., Jacob, D. J., Fisher, J. A., Kim, P. S., Marais, E. A., Zhu, L., et al. (2016). Why do models overestimate surface ozone in the Southeast United States? *Atmospheric Chemistry and Physics*, *16*(21), 13,561–13,577. https://doi.org/10.5194/acp-16-13561-2016

Turner, A. J., & Jacob, D. J. (2015). Balancing aggregation and smoothing errors in inverse models. *Atmospheric Chemistry and Physics*, *15*(12), 7039–7048. https://doi.org/10.5194/acp-15-7039-2015

Wang, Y., Lyapustin, A. I., Privette, J. L., Cook, R. B., SanthanaVannan, S. K., Vermote, E. F., & Schaaf, C. L. (2010). Assessment of biases in MODIS surface reflectance due to Lambertian approximation. *Remote Sensing of Environment*, *114*(11), 2791–2801. https://doi.org/10.1016/j.rse.2010.06.013

Zoogman, P., Liu, X., Suleiman, R. M., Pennington, W. F., Flittner, D. E., Al-Saadi, J. A., et al. (2017). Tropospheric emissions: Monitoring of pollution (TEMPO). *Journal of Quantitative Spectroscopy & Radiative Transfer*, *186*, 17–39. https://doi.org/10.1016/j.jqsrt.2016.05.008